Deep-subwavelength lithography via graphene plasmons

Xiaodong Zeng, Longfei Fan, and M. Suhail Zubairy

Institute for Quantum Science and Engineering (IQSE) and Department of Physics and Astronomy,
Texas A & M University, College Station, Texas 77843-4242, USA

(Received 6 February 2017; published 19 May 2017)

We propose a scheme to overcome diffraction limit in optical lithography via graphene-plasmon (GP) interference. Taking advantage of the novel properties of GPs—tunability, low loss, and extremely large wave number—we can realize lithography with a resolution up to 1/100 wavelength in arbitrary one- and even simple two-dimensional patterns. An advantage of this method is that it works in the linear optics regime and does not require either multiphoton absorption materials or strong intensity lasers.

I. INTRODUCTION

According to the Rayleigh criterion, it is a challenge to improve the resolution of imaging and lithography to be smaller than half wavelength, which is called the Abbe diffraction limit [1]. How to overcome this limit has been an attractive topic for more than a century and has included subwavelength interferometric lithography, which is very important in nanofabrication areas, such as in the semiconductor industry that strives for a miniaturization of their devices. In the past decades, several methods have been developed to improve the spatial resolution beyond the diffraction limit [2–17].

Among these approaches, quantum lithography based on quantum entanglement requires entangled photon number states that are experimentally difficult to generate and sustain [2–5]. To avoid this shortcoming, several classical approaches were developed. However, in these schemes, multiphoton absorption materials [7–9], multi-Λ levels [10,11], or strong intensity lasers [12–15] are required to generate spatial distribution of the atomic population dependent on the field intensity nonlinearly, which is difficult in experiment. As a result, to shorten the field wavelength is the choice to realize smaller patterns. Surface plasmons are electromagnetic excitations associated with charge density waves on the surface of a conduction or a semiconduction object. The amazing property of the surface plasmons is the short wavelength, which can be used in lithography, and a number of related proposals have been presented. These schemes, however, have weak resolution ability and suffer from a fixed lithography pattern for determined plasmonic device [16,17].

Graphene, a single layer of carbon atoms arranged in a honeycomb lattice, is well known for its unique electronic, mechanical, and optical properties [18–33]. Especially, graphene plasmons (GPs) have emerged as a hot topic in recent years due to their tunability, long life and extreme light confinement. The Fermi velocity of the doped graphene is $v_F = 10^6$ m/s, which leads to a wave number that is about two orders larger than that in vacuum. Besides, due to Pauli blocking, doped graphene has low absorption in the midinfrared region. Additionally, the convenient controllability of the carrier density near the Dirac point signifies that the GPs can be manipulated easily, such as by electric voltage and temperature.

In the present work, we propose a scheme to use monolayer graphene to achieve deep-subwavelength lithography with an arbitrary one- or simple two-dimensional pattern. Due to the tunability of graphene, we can control the Fermi level conveniently. Consequently, the conductivity and, as a result, the plasmonic wavelength can be tuned for a determined frequency. Therefore, we can obtain standing wave patterns with tunable periods, which can be used to construct the arbitrary patterns we need. Compared to the previous schemes, this method works in the linear optics region and does not require multiphoton absorption materials or strong intensity lasers.

The paper is organized as follows. In Sec. II, we present the detail of our model and discuss the theory. In Sec. III, we present the simulations and discuss the results. In Sec. IV, we present the concluding remarks.

II. GRAPHENE PLASMONIC DISPERSION RELATION AND FIELD INTENSITY DISTRIBUTION

Our model is schematically shown in Fig. 1(a). The monolayer graphene is placed at $z = 0$ between two dielectric slabs of permittivities ε_1 and ε_2, as shown in the figure. The photoresist material is placed near the bottom slab, the effective permittivity ε_3 has an absorption coefficient and is dependent on the population on level $|e\rangle$. Throughout the paper, we set $\varepsilon_3 = 2 + 0.06i$. The bottom slab cannot only support the graphene sheet, but it can also prevent the photoresist from polluting the graphene. The distance between the graphene and the photoresist, i.e., the thickness of the bottom dielectric slab, is d. The Fermi level of the graphene can be controlled by the gate voltage. Laser beams can illuminate the gratings to excite GPs. The GPs along different directions can construct periodic field intensity patterns that play the key role in our lithography scheme due to their tunable periods. The molecular structure of the photoresist is shown in Fig. 1(b). Initially, the molecules are in the ground state $|g\rangle$. Then a visible laser beam with frequency ω_l excites the molecules to the excited state $|e\rangle$. Afterwards, GPs with frequency ω_p excite the molecules to an ancillary state $|a\rangle$. At the end, a laser with frequency ω_a dissociates the lithography molecules that are in state $|a\rangle$, but not those in other states. The resulting patterns of the photoresist thus depend on the spatial distribution of molecules in state $|a\rangle$.
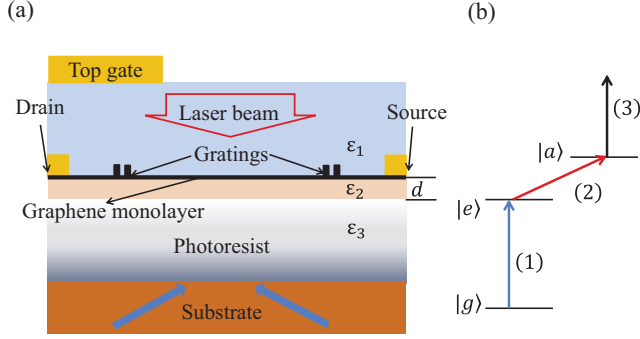
FIG. 1. (a) The diagram of the lithography scheme. The top gate can control the Fermi level of the monolayer graphene. GPs can be generated by the dielectric gratings. Dielectric 1 has permittivity $\varepsilon_1 = 2.0$ and dielectric 2 has permittivity $\varepsilon_2 = 2.0$. (b) The energy structure of the photoresist.

In the long-wavelength limit, the in-plane conductivity of graphene can be described as [21]

$$
\sigma(\omega_p) = \frac{ie^2 E_F}{\pi \hbar^2 (\omega_p + i\tau^{-1})}
$$
$$
+ \frac{e^2}{4\hbar}\left[\Theta(\hbar\omega_p - 2E_F) + \frac{i}{\pi}\ln\left|\frac{\hbar\omega_p - 2E_F}{\hbar\omega_p + 2E_F}\right| \right], \quad (1)
$$

under the random phase approximation (RPA). Here, E_F is the Fermi level, e is the electron charge, and $\Theta(x)$ is a Heaviside step function, where $\Theta(x) = 1$ for $x \geqslant 0$ and $\Theta(x) = 0$ for $x < 0$. In the high doping limit, i.e., $\hbar\omega_p \ll 2E_F$, the conductivity has a Drude form given by the first term of the right-hand side of Eq. (1). τ denotes the momentum relaxation time due to impurities or phonon-mediated scattering. When the frequency is below the optical phonon frequency $\hbar\omega_{op} \approx$ 0.2 eV [23], the phonon-mediated scattering can be neglected. Then τ can be expressed as $\tau = \mu E_F / e v_F^2$. Here, μ is the mobility of graphene charge carriers, whose values can reach 10^4–10^6 cm^2/V s [20]. In this paper, we set the mobility $\mu = 4\times10^4$ cm^2/V s at $E_F = 0.24$ eV and $\mu = 0.64\times10^4$ cm^2/V s at $E_F = 0.6$ eV.

The tunability of graphene results from the controllability of its Fermi level. Near the Dirac point, the magnitude of Fermi level is proportional to the square root of the carrier density n; i.e., $E_F = \hbar v_F \sqrt{\pi n}$. In addition, the carrier density depends on the voltage of the top gate as $V_{GD} = ne/C_g + E_F/e$ [24]. Here, V_{GD} denotes the voltage difference between the top gate and the drain; C_g refers to the charge capability of the system, which depends on the structure size and the properties of the top dielectric. The value of C_g can reach tens of thousandths F/m^2, for example, by using ionic gel as the top dielectric, which can efficiently reduce the operation voltage. In Fig. 2, we plot the Fermi level as a function of V_{GD}. Here, we choose C_g to be $0.025 F/m^2$ [25].

Given the boundary conditions shown in Fig. 1, the plasmonic wave number k_{gp} has the following dispersion relation (see the Appendix):

$$
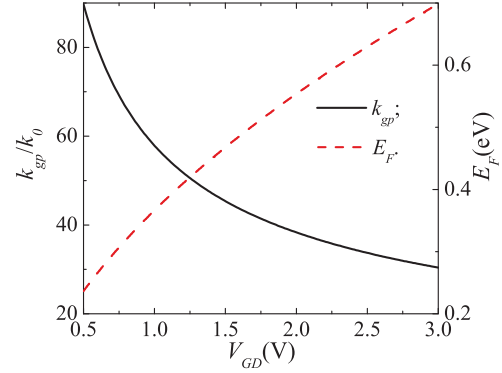1 - \alpha_{21}^p \alpha_{23}^p e^{2i\beta_2 d} = 0. \quad (2)
$$

FIG. 2. The Fermi level as well as the plasmonic wave number as a function of the voltage V_{GD}. Here, the vacuum wavelength of the plasmon is set to be $\lambda_0 = 8$ μm and the thickness d of the bottom dielectric slab is set to be 10 nm.

If we have assumed $\varepsilon_2 = \varepsilon_3$ and neglect the loss, the plasmonic wave number can be approximated by the relation [18]

$$
\text{Re}[k_{gp}(\omega_p)] \approx \frac{(\varepsilon_1 + \varepsilon_2)}{4\alpha} \frac{\omega_p}{\omega_F} k_0, \quad (3)
$$

where $\alpha = e^2/4\pi\hbar\varepsilon_0 c \approx 1/137$ is the fine structure constant and $\omega_F = E_F/\hbar$. In Fig. 2 we plot the plasmonic wave number as a function of V_{GD}, which, due to the electric field, decays exponentially away from the graphene layer and the dielectric 2 consequently limits the highest-resolution ability of the structure. This means that optimizing d is necessary.

For a graphene plasmon along the x direction, the electric field near the graphene is proportional to $(k_{gp}\mathbf{e}_z + \beta_3\mathbf{e}_x)e^{ik_{gp}x}$. Due to the huge value of the plasmonic wave number, the electric fields along the x and z directions have almost the same amplitude but a phase difference $\pi/2$. Two counterpropagation GPs along the x have a z component proportional to $e^{ik_{gp}x}\mathbf{e}_z + e^{-ik_{gp}x}\mathbf{e}_z = 2\cos(k_{gp}x)\mathbf{e}_z$ and an x component proportional to $e^{ik_{gp}x}\mathbf{e}_x - e^{-ik_{gp}x}\mathbf{e}_x = 2\sin(k_{gp}x)\mathbf{e}_x$. As a consequence, the field pattern in the photoresist constructed by the two counterpropagating plasmons along the x direction has a constant intensity. However, due to the interference between incident wave and the plasmons, the total field always shows periodic pattern rather than a constant. For instance, as shown in Fig. 3(a), we assume the gratings are located parallel to each other and homogeneous along the y direction. A TM-polarized wave incident to the gratings has an incident angle ϕ_0. The electric field of the plane wave can be expressed as $(\cos\phi\mathbf{e}_x + \sin\phi\mathbf{e}_z)e^{ik_3\sin\phi x}e^{-i\omega_p t}$, with amplitude set to be 1. Here, ϕ is the refractive angle of the incident plane wave in the photoresist material. The plasmonic electric field distribution is $E_0[\cos(k_{gp}x + \theta)\mathbf{e}_x + \sin(k_{gp}x + \theta)\mathbf{e}_z]e^{-i\omega_p t}$. Here, E_0 is the amplitude multiplied by the relative phase difference between the the incident wave and the plasmonic pattern. θ denotes the position of the pattern and always is dependent on the arrival time difference of the plane wave to the two gratings. If we set $\phi = \pi/4$, the total field intensity can be obtained as

$$
|E_0\cos(k_{gp}x + \theta) + \cos\phi e^{ik_3\sin\phi x}|^2
$$
$$
+ |E_0\sin(k_{gp}x + \theta) + \sin\phi e^{ik_3\sin\phi x}|^2 = 1 + |E_0|^2
$$
$$
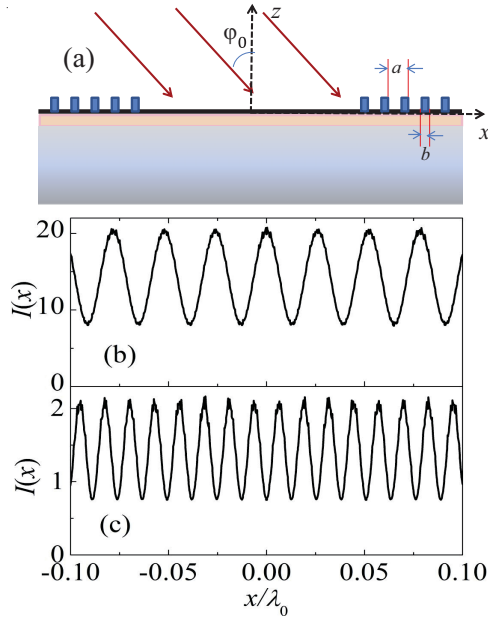+ 2\text{Re}(E_0 e^{i\sqrt{2}k_3 x/2})\cos(k_{gp}x + \theta - \pi/4). \quad (4)
$$

FIG. 3. (a) Two perpendicular located dielectric gratings couple two TM-polarized laser beams to the GPs. The period of the gratings is $a = 720$ nm, the width of the silicon rectangular is $b = 36$ nm, and the relative permittivity of the silicon is 12. Additionally, the distance between the gratings is 6 μm and the height of the silicon rectangle is 150 nm. The field intensity distribution in the photoresist is $V_{GD} = 1.73$ V in (b) and $V_{GD} = 0.56$ V in (c).

As shown in Fig. 2, the plasmonic wave number is tens of times larger than the vacuum wave number; i.e., $k_{gp} \gg \sqrt{2}k_3/2$. The above expression describes a standing wave pattern with an effective period of $2\pi/k_{gp}$ and a background $1 + |E_0|^2$. And, more remarkably, the phase shift $\theta - \pi/4$ in the above equation is dependent on ϕ_0. If we change the angle ϕ_0, we can change the phase shift in a large range. The means that we can obtain sinusoidal as well as cosine patterns, which plays an indispensable role in the arbitrary pattern lithography.

Due to the loss of the graphene and the optical absorption of the photoresist, the field decays strongly along the graphene. In order to realize a periodic pattern with low background, the wave vector matching between the incident field and the GPs is required [28,29], which means

$$k_1 \sin \phi_0 + m\Lambda \approx m\Lambda = \frac{\left(\varepsilon_1^{\text{eff}} + \varepsilon_2\right)}{4\alpha} \frac{\omega_p}{\omega_F} k_0. \quad (5)$$

Here, $m = 1, 2, \ldots$ are integers, and $\Lambda = 2\pi/a$ (a is the period of the grating) is the reciprocal vector of the grating. $\varepsilon_1^{\text{eff}}$ is the average permittivity of the grating which is determined by the duty as well as the grating material's permittivity. The limited number of the grating periods and the loss of the graphene relax the wave vector matching condition. In Figs. 3 and 4, we give some simulation results of the field intensity at $z = -15$ nm in the photoresist by COMSOL Multiphysics. In the simulation, the monolayer graphene is modeled as conductor with thickness 0.5 nm [29]. We can see that near the origin, the field distribution is approximately cosinoidal. Meanwhile, the period of the pattern can be manipulated by
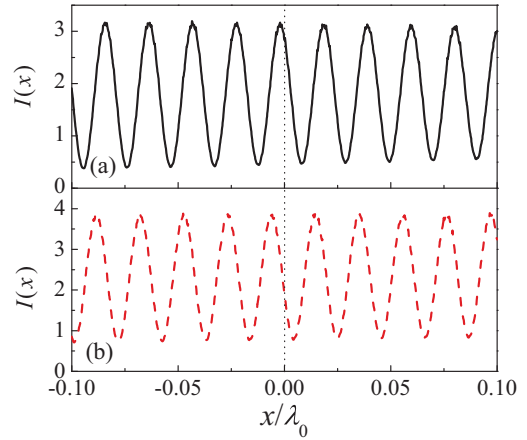

FIG. 4. The field intensity distributions with $V_{GD} = 1.19$ V and incident angles (a) $27°$ and (b) $10°$.

controlling the gate voltage. In Fig. 4, we show that different incident angles induce different pattern positions.

III. LITHOGRAPHY PROCESS AND SIMULATIONS

In the previous section, we showed that periodic field patterns with periods much smaller than the vacuum wavelength can be obtained, which means that we can obtain a deep-subwavelength lithography pattern. Additionally, arbitrary one- and simple two-dimensional lithography patterns can be realized in principle by multiple exposure methods discussed in Refs. [8,34]. In this section, we introduce the details of the lithography scheme and present some simulations.

The mathematic process of obtaining arbitrary patterns lies in that the target pattern can be expanded to a series Fourier components $\sin(kx)$ and $\cos(kx)$. If the Fourier coefficients of $\sin(kx)$ and $\cos(kx)$ are A and B and we can realize regular field intensity patterns $\cos(kx + \theta)$ and $\cos(kx - \theta)$, the coefficient of our patterns are $(A + B)/2\cos(\theta)$ and $(A - B)/2\sin(\theta)$. We can control the incident angle to optimize the positions of the patterns to minimize the lithography noise and deposition.

In a limited-size arbitrary pattern lithography, we just need field patterns with several separated periods. If the size of lithography area is b (or we just etch this area in each time), the periods of the patterns are $b/2n$ ($n = 1, 2 \ldots$ are integers). As a consequence, if we set $b = (\varepsilon_1^{\text{eff}} + \varepsilon_2)a/(\varepsilon_1 + \varepsilon_2)$, the wave vector matching condition [Eq. (5)] and the dispersion relation [Eq. (3)] always can be satisfied even if we change the plasmonic wavelength.

We notice that the minimum effective wave number of the GPs pattern is limited by the maximum Fermi level we can obtain. For example, with the parameters in Fig. 2, the minimum wave number is still rather large, i.e., about $30k_0$. As we know, for a certain lithography pattern we want, the Fourier expansion contains not only high-spatial-frequency components but also low-spatial-frequency components. As a consequence, we still need to generate field intensity pattern with relatively low spatial frequency. Fortunately, the first step in Fig. 1(b) can play this role. Since ω_l lies in the visible region, the standing wave pattern due to two counterpropagation laser
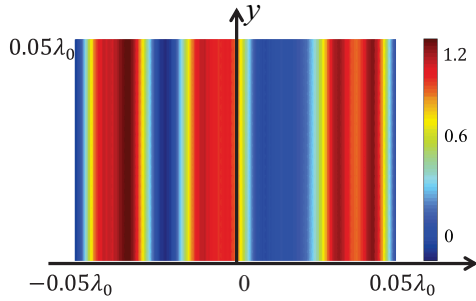
FIG. 5. The simulation of one-dimensional pattern.

beam with frequency ω_l can excite the molecule to excited state $|e\rangle$ with spatial frequency from $0k_0$ to about $27k_0$ when we set the visible laser wavelength to be 600 nm. If we reduce the plasmonic frequency, all the Fourier components can be obtained.

For the lithography of the high-spatial-frequency components shown in Fig. 1, first, we use uniform laser with frequency ω_l to excite all the molecules to state $|e\rangle$. Then we construct a GP pattern to pump the molecules to state $|a\rangle$. As we know, plasmons decay exponentially from the graphene layer. At the beginning, we control the top gate voltage to make the graphene sheet on a small Fermi level, which means a large plasmonic wave number. Afterwards, we enlarge the Fermi level to realize a smaller plasmonic wave number. For the lithography of the low-spatial-frequency components, after the standing wave pattern with frequency ω_l excites the molecules, a uniform laser with frequency ω_p pumps all the molecules in state $|e\rangle$ to state $|a\rangle$. We carry out this process step by step to complete the whole lithography process.

In Fig. 5, we present a one-dimensional example. The simulation shows that a high-quality lithography pattern with deep-subwavelength resolution can be obtained. Due to the dissipation of the graphene and the photoresist, the field patterns are always not perfectly regular, which induces some error in the lithography result. However, this error can be neglected if we just etch a small region one time. We can follow the idea in Ref. [12] to control the lithography area by using the photoetching laser. After one time of the lithography, we move the laser spot to another area. At the same time, we control the incident angle and even the spatial field intensity distribution of the incident wave to construct a standing field pattern in the new area. The lithography of the new area can be realized by the same processes as before. Finally, large area lithography can be achieved by scanning the whole area by the photoetching laser. In addition, due to the fact that the background $1 + |E_0|^2$ appears in Eq. (4), there is an additional penalty deposition Q which depends on the Fourier coefficients [8,34]. In the example of Fig. 4, $Q \approx 2h$, where h is the height of the pattern and is set to be 1 in the figure. Because the plamonic intensity decays exponentially from the graphene, the field distribution far away to the graphene has larger background, as shown in Eq. (4). This means that the total deposition will be larger if we consider real lithography process with thick photoresist. For a two-dimensional pattern, the number of Fourier components is squared. As a consequence, the deposition will be too large. Meanwhile, the noise resulting from the loss of the graphene

and photoresist will be also too large. However, for simple two-dimensional patterns, such as gridding structure [35], this proposal may be valid.

This proposal also can be utilized in imaging, where large background deposition is not a serious problem. Compared to our previous work on imaging [18], this scheme may be more practical, because it is more convenient to manipulate the gate voltage than control the angle of two GPs.

In our model, high-quality graphene with high mobility is required, which can make the standing plasmonic pattern more regular and also increase the size of a time lithography area. As the fabrication process in graphene improves, the mobility of graphene can be made higher and higher. As an example, shown in [36], the mobility can reach 4×10^4 cm^2/V s at a carrier density 4.5×10^{12} cm^{-2} at room temperature, which corresponds to a Fermi level of 0.24 eV. This means $\omega_p/\tau = \mathrm{Re}(k_{gp})/\mathrm{Im}(k_{gp}) \approx 240$. As a consequence, the graphene plasmon can propagate 40 plasmonic wavelengths. At low temperature, the mobility even can be several times higher. These experimental results agree with the theoretical predications based on acoustic phonon in [37], where the mobility and carrier are related as $\mu \propto n^{-1}$. In later works, ultrahigh-mobility and large-scale graphene from chemical vapor deposition are realized [38,39], and the mobility is comparable with exfoliated graphene. These advancements in graphene fabrication make our scheme realistic. Additionally, it is also important to design the dielectric gratings appropriately to increase the efficiency of coupling incident waves to GPs, which can decrease the background deposition.

Comparing with the GPs, the surface plasmons based on metal film have symmetric and antisymmetric eigenmodes. The symmetric mode has a small wave number associated with low-resolution ability. The antisymmetric mode has a relatively large wave number. However, this mode always is accompanied by large dissipation [40], which means a small ratio between the real part and the imaginary part of the plasmonic wave vector is harmful to be used in arbitrary pattern lithography or imaging.

IV. CONCLUSION

In the present paper, we propose a scheme to realize deep-subwavelength lithography via monolayer graphene, which may be useful in nanodevice fabrication. Taking advantage of the ultrahigh field confinement and tunability of GPs, we can realize optical lithography with tens of nanometers resolution even through the real plasmonic energy frequency is in the midinfrared region. Compared to the previous schemes, where strong lasers are required or fixed lithography pattern for determined plasmonic device, this scheme works in the linear optics region and we can obtain arbitrary structure by manipulating the voltage of the top gate.

APPENDIX: DERIVATIONS OF EQ. (2)

As shown in Fig. 1, we denote the interface between dielectrics 1 and 2 as interface A and the interface between dielectrics 2 and 3 as interface B. Here, we solve the dispersion relation of TM-polarized surface plasmonic modes supported by the structure.

Due to the continuity of the electric field on the interfaces, we assume the electric field to be parallel to interface A as E_A and the electric field component to be parallel to interface B as E_B. The components up- and down-prorogation in dielectric 2 are E_u and E_d, respectively. They have the relations

$$-E_u + E_d = E_A; \tag{A1}$$

$$-E_u e^{-i\beta_2 d} + E_d e^{i\beta_2 d} = E_B. \tag{A2}$$

Here $k_i = \varepsilon_i k_0$ $(i = 1,2,3)$ are the wave numbers in dielectric i, where $k_0 = \omega_p/c$ and c is the vacuum light velocity. $\beta_i = \sqrt{k_i^2 - k_{gp}^2}$ are the wave-number components perpendicular to the graphene. By using the Maxwell equations, it is easily to obtain the magnetic fields on the interface. The magnetic field above interface A is $H_{A1} = E_A k_1 \sqrt{\varepsilon_1} \sqrt{\varepsilon_0}/\sqrt{\mu_0}\beta_1$, while the magnetic field below

interface A is $H_{A2} = (E_u + E_d)k_2\sqrt{\varepsilon_2}\sqrt{\varepsilon_0}/\sqrt{\mu_0}\beta_0$. Here, ε_0 and μ_0 are the vacuum permittivity and permeability, respectively. The magnetic fields have the relation

$$H_{A1} - H_{A2} = \sigma E_A, \tag{A3}$$

which means

$$(E_u + E_d)k_2\sqrt{\varepsilon_2}/\beta_2 - E_A k_1\sqrt{\varepsilon_1}/\beta_1 = \sigma E_A. \tag{A4}$$

Similarly, the magnetic fields on interface B have the relation

$$(E_u e^{-i\beta_2 d} + E_d e^{i\beta_2 d})k_2\sqrt{\varepsilon_2}/\beta_2 = E_B k_3\sqrt{\varepsilon_3}/\beta_3. \tag{A5}$$

Combining Eqs. (A1)–(A5), we can obtain Eq. (2). Here,

$$\alpha_{21}^p = \frac{\varepsilon_1\beta_2 - \varepsilon_2\beta_1 + \sigma\beta_1\beta_2/\sqrt{\mu_0}k_0}{\varepsilon_1\beta_2 + \varepsilon_2\beta_1 + \sigma\beta_1\beta_2/\sqrt{\mu_0}k_0} \tag{A6}$$

and

$$\alpha_{23}^p = \frac{\varepsilon_3\beta_2 - \varepsilon_2\beta_3}{\varepsilon_3\beta_2 + \varepsilon_2\beta_3}. \tag{A7}$$

As shown in Ref. [21], the physical meaning of α_{21}^p is the reflection coefficient of a TM-polarized plane wave incident from dielectric 2 to dielectric 1 with a monolayer graphene between them, while α_{23}^p is the reflection coefficient of a TM-polarized plane wave incident from dielectric 2 to dielectric 3.

[1] C. Mack, *Fundamental Optical Principles of Lithography: The Science of Microfabrication* (Wiley & Sons, West Sussex, UK, 2007).

[2] C. Williams, P. Kok, H. Lee, and J. P. Dowling, Inf. Forschr. Entwickl. **21**, 73 (2006).

[3] A. N. Boto, P. Kok, D. S. Abrams, S. L. Braunstein, C. P. Williams, and J. P. Dowling, Phys. Rev. Lett. **85**, 2733 (2000).

[4] M. D'Angelo, M. V. Chekhova, and Y. Shih, Phys. Rev. Lett. **87**, 013602 (2001).

[5] G. S. Agarwal, R. W. Boyd, E. M. Nagasako, and S. J. Bentley, Phys. Rev. Lett. **86**, 1389 (2001).

[6] S. J. Bentley and R. W. Boyd, Opt. Express **12**, 5735 (2004).

[7] P. R. Hemmer, A. Muthukrishnan, M. O. Scully, and M. S. Zubairy, Phys. Rev. Lett. **96**, 163603 (2006).

[8] Q. Sun, P. R. Hemmer, and M. S. Zubairy, Phys. Rev. A **75**, 065803 (2007).

[9] W. Ge, P. R. Hemmer, and M. S. Zubairy, Phys. Rev. A **87**, 023818 (2013).

[10] M. Kiffner, J. Evers, and M. S. Zubairy, Phys. Rev. Lett. **100**, 073602 (2008).

[11] H. Li, V. A. Sautenkov, M. M. Kash, A. V. Sokolov, G. R. Welch, Y. V. Rostovtsev, M. S. Zubairy, and M. O. Scully, Phys. Rev. A **78**, 013803 (2008).

[12] Z. Liao, M. Al-Amri, and M. S. Zubairy, Phys. Rev. Lett. **105**, 183601 (2010).

[13] Z. Liao, M. Al-Amri, T. Becker, W. P. Schleich, M. O. Scully, and M. S. Zubairy, Phys. Rev. A **87**, 023405 (2013).

[14] Z. Liao, M. Al-Amri, and M. S. Zubairy, Phys. Rev. A **88**, 053809 (2013).

[15] J. Rui, Y. Jiang, G. P. Lu, M. J. Zhu, B. Zhao, X. H. Bao, and J. W. Pan, Phys. Rev. A **93**, 033837 (2016).

[16] W. Srituravanich, N. Fang, C. Sun, Q. Luo, and X. Zhang, Nano Lett. **4**, 1085 (2004).

[17] Z. Xie, W. Yu, T. Wang, H. Zhang, Y. Fu, H. Liu, F. Li, Z. Lu, and Q. Sun, Plasmonics **6**, 565 (2011).

[18] X. Zeng, M. Al-Amri, and M. S. Zubairy, Phys. Rev. B **90**, 235418 (2014).

[19] A. H. Castro Neto, F. Guinea, N. M. R. Peres, K. S. Novoselov, and A. K. Geim, Rev. Mod. Phys. **81**, 109 (2009).

[20] T. Low and P. Avouris, ACS Nano **8**, 1086 (2014).

[21] F. H. L. Koppens, D. E. Chang, and F. J. G. de Abajo, Nano Lett. **11**, 3370 (2011).

[22] L. Ju, B. Geng, J. Horng, C. Girit, M. Martin, Z. Hao, H. A. Bechtel, X. Liang, A. Zettl, Y. R. Shen, and F. Wang, Nat. Nanotechnol. **6**, 630 (2011).

[23] M. Gullans, D. E. Chang, F. H. L. Koppens, F. J. G. de Abajo, and M. D. Lukin, Phys. Rev. Lett. **111**, 247401 (2013).

[24] V. Thareja, J. H. Kang, H. T. Yuan, K. M. Milaninia, H. Y. Hwang, Y. Cui, P. G. Kik, and M. L. Brongersma, Nano Lett. **15**, 1570 (2015).

[25] Z. Fang, S. Thongrattanasiri, A. Schlather, Z. Liu, L. Ma, Y. Wang, P. M. Ajayan, P. Nordlander, N. J. Halas, and F. J. G. de Abajo, ACS Nano **7**, 2388 (2013).

[26] A. N. Grigorenko, M. Polini, and K. S. Novoselov, Nat. Photon. **6**, 749 (2012).

[27] A. Vakil and N. Engheta, Science **332**, 1291 (2011).

[28] T. R. Zhan, F. Y. Zhao, X. H. Hu, X. H. Liu, and J. Zi, Phys. Rev. B **86**, 165416 (2012).

[29] W. Gao, J. Shu, C. Qiu, and Q. Xu, ACS Nano **6**, 7806 (2012).

[30] B. Wunsch, T. Stauber, F. Sols, and F. Guinea, New J. Phys. **8**, 318 (2006).

[31] E. H. Hwang and S. D. Sarma, Phys. Rev. B **75**, 205418 (2007).

[32] M. Jablan, H. Buljan, and M. Soljaċić, Phys. Rev. B **80**, 245435 (2009).

[33] X. Zeng, Z. Liao, M. Al-amri, and M. S. Zubairy, Europhys. Lett. **115**, 14002 (2016).

[34] H. J. Levinson, *Principles of Lithography* (SPIE, Bellingham, WA, 2001).

[35] A. A. Tseng, *Nanofabrication: Fundamentals and Applications* (World Scientific, Singapore, 2008).

[36] L. Wang, I. Meric, P. Y. Huang, Q. Gao, Y. Gao, H. Tran, T. Taniguchi, K. Watanabe, L. M. Campos, D. A. Muller, J. Guo,

P. Kim, J. Hone, K. L. Shepard, and C. R. Dean, Science **342**, 614 (2013).

[37] E. H. Hwang and S. D. Sarma, Phys. Rev. B **77**, 115449 (2008).

[38] L. Banszerus, M. Schmitz, S. Engels, J. Dauber, M. Oellers, F. Haupt, K. Watanabe, T. Taniguchi, B. Beschoten, and C. Stampfer, Sci. Adv. **1**, e1500222 (2015).

[39] L. Banszerus, M. Schmitz, S. Engels, M. Oellers, K. Watanabe, T. Taniguchi, B. Beschoten, and C. Stampfer, Nano Lett. **16**, 1387 (2016)

[40] B. Wang, X. Zhang, F. J. Garcia-Vidal, X. C. Yuan, and J. H. Teng, Phys. Rev. Lett. **109**, 073901 (2012).